



Turbulence in the Strongly Heterogeneous Near-Surface Boundary Layer over Patchy Snow

Michael Haugeneder¹ · Michael Lehning¹ · Ivana Stiperski² · Dylan Reynolds¹ · Rebecca Mott¹

Received: 23 June 2023 / Accepted: 28 December 2023 / Published online: 22 January 2024
© The Author(s) 2024

Abstract

The near-surface boundary layer above patchy snow cover in mountainous terrain is characterized by a highly complex interplay of various flows on multiple scales. In this study, we present data from a comprehensive field campaign that cover a period of 21 days of the ablation season in an alpine valley, from continuous snow cover until complete melt out. We recorded near-surface eddy covariance data at different heights and investigated spectral decompositions. The topographic setting led to the categorisation of flows into up and down valley flows, with a down valley Föhn event in the middle of the observation period. Our findings reveal that the snow cover fraction is a major driver for the structure and dynamics of the atmospheric layer adjacent to the snow surface. With bare ground emerging, stable internal boundary layers (SIBL) developed over the snow. As the snow coverage decreased, the depth of the SIBL decreased below 1 m and spectra of air temperature variance showed a transition towards turbulent time scales, which were caused by the intermittent advection of shallow plumes of warm air over the snow surface. The intermittent advection could also be observed visually with high spatio-temporal resolution measurements using a thermal infrared camera. While the shallow advection only affected the lowest measurement level at 0.3 m, the measurements above at 1 m, 2 m, and 3 m indicate that the distribution of eddy size and, thus, the turbulence structure, did not distinctly change with height.

✉ Michael Haugeneder
michael.haugeneder@slf.ch

Michael Lehning
lehning@slf.ch

Ivana Stiperski
ivana.stiperski@uibk.ac.at

Dylan Reynolds
dylan.reynolds@slf.ch

Rebecca Mott
mott@slf.ch

¹ WSL-Institute for Snow and Avalanche Research SLF, Davos, Switzerland

² Department of Atmospheric and Cryospheric Sciences, University of Innsbruck, Innsbruck, Austria

Keywords Buoyancy flux · Internal boundary layer · Multi-resolution flux decomposition · Patchy snow cover · Surface–atmosphere interaction · Temperature variance · Turbulence kinetic energy

1 Introduction

The exchange of energy, mass, and momentum between the atmosphere and the underlying surface is driven by processes in the Atmospheric Boundary Layer (ABL). Stull (1988) defines it as “that part of the troposphere that is directly influenced by the presence of the earth’s surface and responds to surface forcing with a timescale of about an hour or less”. Due to its significance for understanding, modelling, and predicting weather, it has been the focus of many studies. Due to radiative cooling in clear sky conditions or advection of warm air over a cold surface, stable boundary layers develop. This is especially the case in the presence of snow covering the surface (Schlögl et al. 2017). The stably stratified layer attenuates or even shuts down any turbulent motion. Compared to convective boundary layers, their stable counterparts are less well understood. Interactions with larger, submeso scale motions lead to non-stationary intermittent turbulence (Mahrt 2014).

Similar to the ABL, Lehner and Rotach (2018) define the Mountain Boundary Layer (MBL) over complex topography. The MBL influences the flow on various scales ranging from $\mathcal{O}(10^2 \text{ m})$ to $\mathcal{O}(10^6 \text{ m})$ (Serafin et al. 2018). On a mountain-range scale, forced dynamic lifting or acceleration of atmospheric flow induces phenomena such as Föhn (Drobinski et al. 2007; Jansing et al. 2022). On smaller scales, valleys and ridges also interact with the flow by deflecting the flow direction to follow the valley axis. Flows above the terrain with a cross valley direction accordingly change direction closer to the surface (Whiteman and Doran 1993; Zardi and Whiteman 2013; Jackson et al. 2013). Furthermore, differential heating leads to the development of valley wind systems. During the day, enhanced warming of the valley atmosphere leads to a local low pressure and up valley flow. In the evening, pronounced cooling reverses the valley flow to down valley (Schmidli 2013). The same effects occur on a slope scale. Terrain features like slope angle and exposition induce local differences in the surface energy budget, influencing the temperature of the adjacent air. Slope winds compensate for the resulting buoyancy-driven pressure heterogeneities. With incoming radiation, slopes heat up, and up slope (anabatic) winds develop. Cooling near-surface air by the surface causes downward slope (katabatic) winds. Compared to valley flows, slope flows react much quicker to changes in the surface energy balance as shading of the incoming radiation by clouds or terrain can happen quickly (Nadeau et al. 2013; Zardi and Whiteman 2013). Interaction between flows at all scales and superposition with the synoptic flow adds complexity to the MBL (Zängl 2009).

Not only the topography but also the surface heterogeneity leaves its fingerprint in the atmospheric flow. Surfaces of alternating aerodynamic roughness length, surface temperature, and surface moisture lead to spatially highly heterogeneous turbulent heat and momentum fluxes (Rotach et al. 2015; Goger et al. 2022).

In spring, bare patches arise in the mountainous snow cover. The lower surface albedo leads to an increased energy input by radiation and, thus, to ground heating. However, the melting snow pack’s surface temperature is limited to 0°C , resulting in a substantial surface temperature heterogeneity. This heterogeneity of the surface influences the near-surface atmosphere. Regions of opposite atmospheric stability and sensible heat flux direction develop within just a few meters of lateral distance (Mott et al. 2018).

The advection of warm air leads to the development of a stable internal boundary layer (SIBL) adjacent to the snow surface (Garratt 1990). The SIBL height is characterized by the transition from downward sensible heat fluxes within the SIBL to upward heat fluxes above (Mott et al. 2017). The strong near-surface stability dampens heat fluxes and thus has an impact on the energy balance of snow. During patchy snow cover, depending on the meteorological conditions, heat fluxes contribute up to 30% to the available energy for melt (Pohl et al. 2006; Harder et al. 2017; Schlögl et al. 2018a, b). Above bare ground, however, the high surface temperatures induce the development of heated, convective near-surface atmospheric layers. Additionally, Harder et al. (2017) illustrated the importance of latent heat advection, especially with the presence of upwind ponded water. Despite the impact on snow cover modelling, only a few experimental studies of the interaction between the near-surface atmosphere and melting snow cover have been carried out in the past years (for example Granger et al. 2006; Fujita et al. 2010; Mott et al. 2013; Harder et al. 2017; Mott et al. 2017; Schlögl et al. 2018b; van der Valk et al. 2022).

To address the existing lack of extensive experimental data, we conducted a comprehensive field campaign in an alpine catchment during patchy snow cover. The experiment has been designed to be able to quantify the processes and relevant time- and length scales. Using various measurement techniques, we aim to answer the following questions:

- How do buoyancy fluxes, turbulence kinetic energy, temperature variance, and their time scales change with a decreasing snow cover fraction throughout the ablation period?
- How do the fluxes and their time scales change when approaching the partly snow covered surface? How do they differ at different measurement levels (0.3 m, 1 m, 2 m, and 3 m)?

The paper is structured as follows: The second section gives an overview of the experimental set-up and the applied methods for processing the data. Section 3 describes the meteorological conditions and prevailing flow regimes. After describing how we separated turbulent from non turbulent motions in Sect. 4, Sect. 5 analyzes the development of the near-surface boundary layer during the observation period. Additionally, we elaborate on the vertical structure of turbulence close to the surface. Finally, conclusions are drawn in Sect. 6.

2 Methods

2.1 Study Site and Data Collection

We collected experimental data at the flat Dürrboden in the upper Dischma valley (Fig. 1) close to Davos (Switzerland) from 21 May 2021 to 11 June 2021.

The Dischma valley is an alpine valley with its valley axis in southeast–northwest direction. It has been comprehensively investigated for multiple observational and modelling studies (Lehning et al. 2006; Bavay et al. 2009; Brauchli et al. 2017; Wever et al. 2017; Schlögl et al. 2018a, b; Gerber et al. 2019; Carletti et al. 2022; Reynolds et al. 2023). Slopes enclose the valley floor with an elevation difference of around 1000 m. Piz Grialetsch and Scalettahorn form the boundary of the catchment area towards the south–southeast. These peaks have long-lasting snow fields and a small glacier on their northern slopes, visible on the bottom right of the map in Fig. 1. On the ridge, at an elevation of 3035 m a.s.l. an automatic weather station records meteorological data. The data are used to classify Föhn periods in Sect. 3.2. At an altitude of 2010 m a.s.l., the flat area of Dürrboden is covered by alpine meadow and accessible by a maintained road. The orthophoto (Fig. 1 right) shows the Dürrboden area on 3 June 2021.

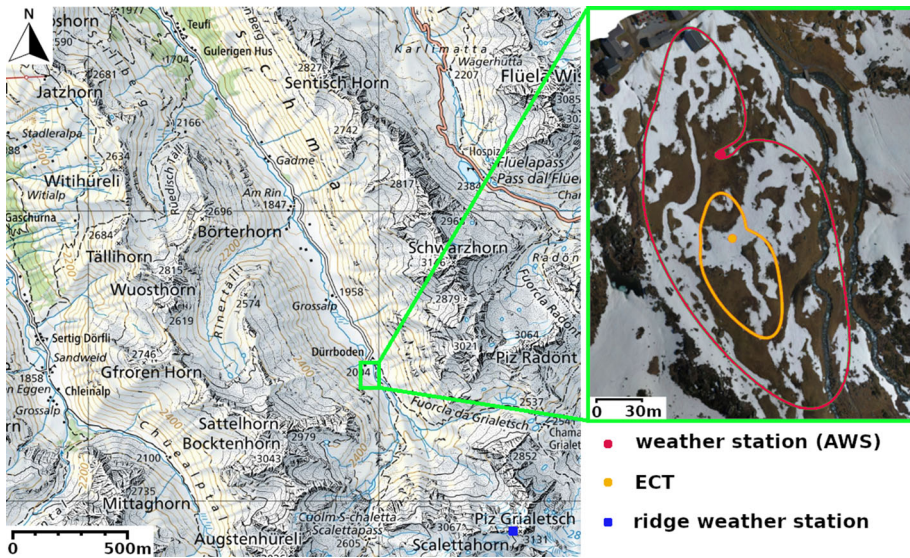


Fig. 1 Topographic map of Dischma valley end close to Davos (Switzerland). In the green box, an orthophoto (3 June 2021) obtained from an Uncrewed Aerial Vehicle shows the flat study site with the measurement stations including an automatic weather station (AWS). Additionally, the 70% climatological flux footprints according to Kljun et al. (2015) are shown for a 5 m measurement at the AWS (red line) and a 2 m measurement at the eddy covariance measurement tower (ECT) (orange line). Furthermore, a blue dot indicates the location of an automatic weather station at the ridge close to Piz Grialetsch

The location of an automatic weather station (AWS) and a movable eddy covariance measurement tower (ECT) is also marked on the orthophoto in Fig. 1. Figure 2 shows a picture of the two measurement stations. The sensors used for the analysis in the present study are highlighted and their specifications are further described in Table 1. All sensors on the ECT were sampled at 20 Hz using a single data logger.

The AWS was installed at a fixed position throughout the whole campaign. At the beginning of the observation period, the surface below was still snow covered. However, a small bare patch below the station emerged on 22 May. It gradually expanded to a radius of ≈ 2 m on 30 May. Afterwards, the bare patch quickly grew (see orthophoto on 3 June in Fig. 1).

Additionally, Uncrewed Aerial Vehicle (UAV) flights were conducted on multiple days to obtain orthorectified areal overview photos. Figure 3 shows captured orthophotos revealing the snow cover distribution throughout the campaign.

The AWS and the ECT positions are indicated by circles. Applying a pixel colour value threshold on the blue band of the orthophotos yields information on the snow cover fraction (Eker et al. 2019). Snow covered pixels exceed the threshold, while bare pixels stay below.

We repositioned the ECT once according to the snow distribution. We expect that for up valley flows, the sensors at the ECT characterized the near-surface atmospheric layer above the upwind edge of a snow patch. Until 31 May, when more bare patches arose, both were positioned close to the AWS. At noon of 31 May, we relocated the ECT to a second position approximately 80 m south-south-west, where it remained during the rest of the observation period. We relocated the ECT such, that the distance to the upwind edge of the snow patch before and after relocation was the same. Thus, we expect no influence on the continuity of the data. The two positions of the ECT throughout the campaign are indicated by the

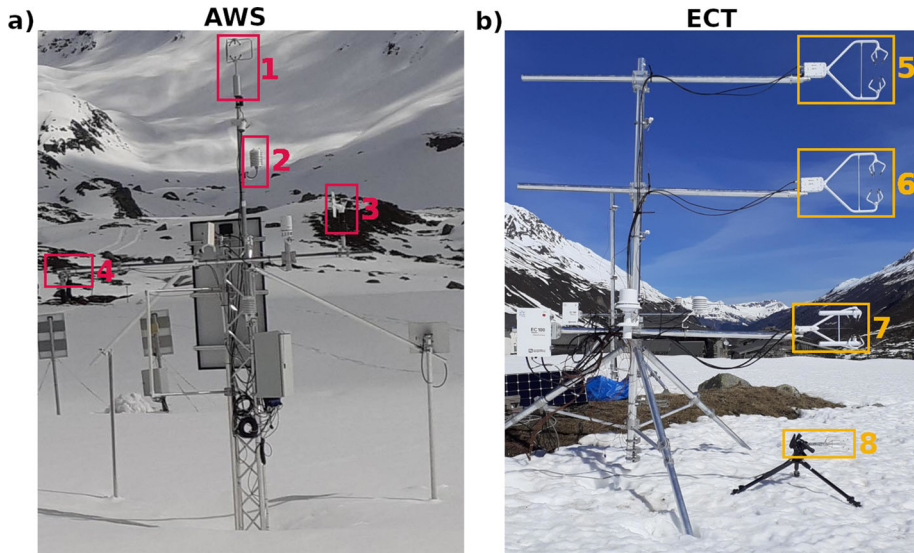


Fig. 2 **a** The automatic weather station (AWS). **b** The eddy covariance measurement tower (ECT) and a short-path ultrasonic anemometer. Instruments used for the present study are highlighted with the corresponding descriptions and specifications in Table 1. The pictures were taken on 20 May 2021 (AWS) and 28 May 2021 (ECT)

Table 1 Sensors used for the present study

Nr.	Height [m]	Model	Description
1	5.0	81000 Ultrasonic Anemometer, YOUNG ^a	EC sensor
2	4.0	CS215-L Campbell Scientific ^b	T_{air} and RH sensor
3	3.5	05103 Wind Monitor, YOUNG ^a	Propeller anemometer
4	3.1	SN-500-SS, Apogee Instruments ^c	Net radiometer
5	3	CSAT3B, Campbell Scientific ^b	EC sensor
6	2	CSAT3B, Campbell Scientific ^b	EC sensor
7	1	IRGASON, Campbell Scientific ^b	EC sensor and gas analyser
8	0.3	DA-700, Sonic Corporation ^d	Short-path EC sensor

See Fig. 2 for a picture and the numbering of the sensors

^a YOUNG, Traverse City, Michigan, USA

^b Campbell Scientific, Logan, Utah, USA

^c Apogee Instruments, Logan, Utah, USA

^d Sonic Corporation, Tokyo, Japan

orange circles in Fig. 3. As the snow cover decreased, the transition line from bare ground to snow approached the ECT. However, the ECT remained above the snow until the end of the observation period.

In Fig. 1, we present the 70% climatological flux footprints for the final position of the ECT from 31 May to 11 June. The climatological flux footprints aggregate flux footprints during the entire observation period. We use the parameterization described in Kljun et al. (2015). The parameterization results from a Lagrangian footprint model using readily available variables like surface roughness, mean wind speed, shear velocity, and lateral wind speed fluctuations.

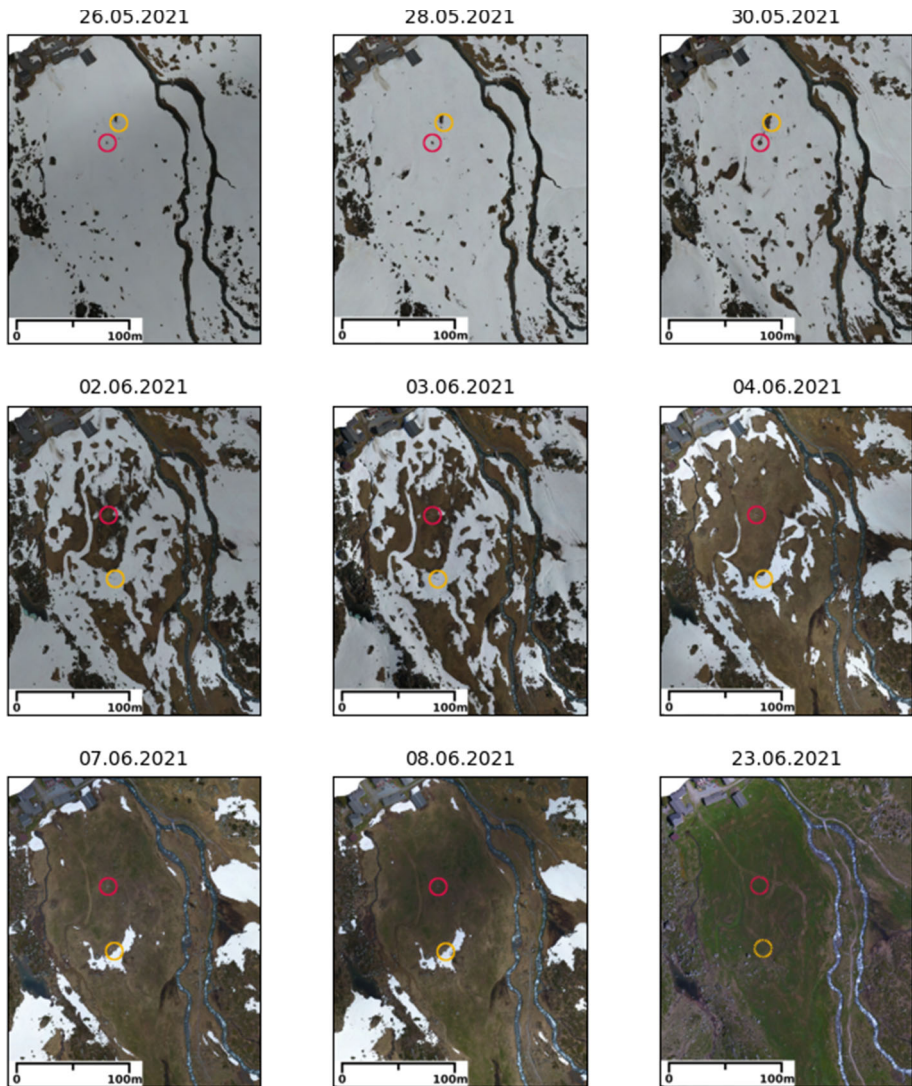


Fig. 3 Orthophotos captured by the UAV during the observation period. The red circles mark the position of the AWS, the orange circles the position of the ECT. The last image captured on 23 May 2021 is a snow off reference. The stations were already dismantled. Therefore, the last position of the stations is indicated by the dotted circles

The orange footprint represents the 3 m measurement at the ECT, while the green footprint represents the 5 m measurement at the AWS. The analysis shows that southerly (down valley) winds dominate the footprints with a smaller contribution from northerly (up valley) winds. For the 5 m measurement, the 70% footprint covers the entire Dürrboden area. The buildings 120 m north of the setup do not substantially disturb the measurements.

From 1 June 0600 LT (LT = local time = UTC + 2 h) to 2 June 1200 LT a portable short-path EC sensor (“8” in Fig. 2 and Table 1) was installed at the ECT at a height of 0.3 m above the snow surface.

In addition to the eddy covariance measurement, we deployed the setup described in Haugeneder et al. (2023). Following their methodology, we recorded sequences of thermal infrared frames of thin synthetic screens vertically deployed across the transition from bare ground to snow. The screens cover a horizontal distance of 6 m and a height of 2 m. Their surface temperature serves as a proxy for local air temperature. The measurements offer a spatio-temporal resolution of 0.6 cm and 30 Hz. The data are presented in Figs. 8 and 9. The shown excerpts stem from a sequence recorded on 31 May 1435LT–1455LT in direct vicinity of the ECT position indicated in Fig. 1.

2.2 EC Data Preparation

The presence of a heterogeneous surface and steep slopes requires special attention in the EC data treatment (Stiperski and Rotach 2016). In the following, we describe the post processing steps to remove artefacts and obtain reliable fluxes. Initially, the diagnostic flags set by the instrument were checked, and suspicious records were flagged as Not-a-Number (NaN). Subsequently, the data were compared to physical limits to remove non-physical values. Additionally, a despiking algorithm, as described by Sigmund et al. (2022), was applied, which considers that spikes often coincide in multiple variables. Next, intervals of NaNs shorter than one second were filled using linear interpolation, reducing the gaps and simplifying posterior flux calculations. Finally, the data were double rotated in 30 min blocks. The double rotation ensures that the u axis is aligned with the mean horizontal wind direction and the mean vertical wind speed vanishes ($\bar{w} = 0$).

To perform a general quality analysis of the EC data, we checked Fourier spectra for the presence of an inertial subrange. Within the inertial subrange, the $\log(f)$ – $\log(fS(f))$ diagram exhibits a $-\frac{2}{3}$ slope (Kolmogorov 1941; Stull 1988). The Fourier spectra in Online Resource 1 for all sensors indicate the existence of the inertial subrange with its characteristic slope suggesting a good quality of the measured data on all EC sensors.

To calculate fluxes, the timescale separating turbulence from submeso scale motions required for Reynolds averaging was determined using a Multi-Resolution Flux Decomposition (see Sect. 2.3) (Howell and Mahrt 1997; Vickers and Mahrt 2003). The results are presented in Sect. 4. For a qualitative description of the difference between turbulence and submeso scale motions see Sect. 4 and 5 and Fig. 2 in Mahrt (2014). $w'T'_s$ denotes the buoyancy flux with a downward flux defined as negative (stable conditions). T_s is the virtual temperature measured by the sonic anemometers containing effects of moisture (Schotanus et al. 1983). From the diagonal entries of the Reynolds stress tensor, turbulence kinetic energy e is calculated as:

$$e = \frac{1}{2} \left(\overline{u'u'} + \overline{v'v'} + \overline{w'w'} \right). \quad (1)$$

In order to explain measured air temperature variances in the strongly stable near-surface layer, we utilize the concept of turbulence potential energy. According to Zilitinkevich et al. (2007), in stable boundary layers, the total turbulence energy is comprised of e , and the turbulence potential energy:

$$E_p = \frac{1}{2} \left(\frac{\beta}{N} \right)^2 \langle \Theta^2 \rangle \propto \overline{(T'_s)^2}, \quad (2)$$

with the buoyancy parameter $\beta = \frac{g}{T_0}$ (gravitational acceleration g and a reference temperature T_0). N denotes the Brunt–Väisälä frequency $N = \left(\beta \frac{\partial \Theta}{\partial z} \right)^{\frac{1}{2}}$, Θ the mean virtual potential

temperature, and z the height above the surface. In unstable conditions, the Brunt–Väisälä frequency becomes imaginary. Therefore, E_p is only defined in stable conditions. In the present study, the proportionality of E_p with the variance of the measured sonic temperature is important.

2.3 Multi-Resolution Flux Decomposition

The Multi-Resolution Flux Decomposition (MRD) is a powerful tool to gain spectral information from a time series data set (Howell and Mahrt 1997). MRD is a wavelet decomposition into dyadic scales with a constant basis function (Vickers and Mahrt 2003). The decomposition offers scale-wise information on fluxes while preserving Reynolds averaging rules. Unlike the Fourier Decomposition, it is not based on the assumption of infinite temporal periodicity of the data. This periodicity includes both turbulent events and the temporal separation between events. Turbulence in general does not fulfil the periodicity assumption. Therefore, MRD is preferred over Fourier decomposition. According to Vickers and Mahrt (2003) the MRD cospectrum of two turbulent time series u_i and ϕ_i , $i = 1, 2, \dots, 2^M$ at scale $m + 1$, $m = 0, 1, \dots, M - 1$ is given by:

$$C_{u\phi}(m + 1) = \frac{1}{2^{M-m}} \sum_{n=1}^{2^{M-m}} \bar{u}_n(m) \bar{\phi}_n(m), \quad (3)$$

with $\bar{u}_n(m)$ (similar for $\bar{\phi}_n(m)$) the mean of all 2^m non-overlapping segments of length 2^{M-m} :

$$\bar{u}_n(m) = \frac{1}{2^m} \sum_{i=(n-1)2^m+1}^{n2^m} ur_i(m), \quad n = 1, \dots, 2^{M-m}, \quad (4)$$

$ur_i(m)$ is the residual time series where segment averages of width $> 2^m$ have been subtracted. An MRD is obtained recursively starting with the average over the complete time series ($m = M$; no $C_{u\phi}(M)$ is calculated). Subsequently, the average is removed from the time series to obtain $ur_i(M-1)$ and (3) and (4) are evaluated for $m = M-1$. At last, $C_{u\phi}(0)$ is determined by the fluctuations of single data points about 2-point means. For a visualisation see Fig. 1 in Vickers and Mahrt (2003). The flux calculated using a specific Reynolds averaging time (2^m data points) can be obtained by summing the spectral contributions for scales $\leq m$.

Applying MRDs for multiple windows shifted by Δi data points (corresponding to a time shift of Δt) a time series of arbitrary length l , i.e. $l \neq 2^M$, can be decomposed. Furthermore, it allows for illustrating the change of the MRD with time, which enables observing changes in the turbulence structure from hours to days. Especially in the presented case of a highly heterogeneous near-surface atmospheric layer, much information can be gained from the temporal evolution of the cospectra.

The orthogonal decomposition (non-overlapping averaging segments) is sensitive to a temporal shift of the data. Especially for near-surface turbulence above a strongly heterogeneous surface, the cospectrum at a given scale depends on the position of events at that scale relative to the averaging segments boundaries (Howell and Mahrt 1997). To overcome this drawback, the non-orthogonal MRD uses overlapping averaging segments. In this study consecutive segments are shifted by 1 record yielding maximum overlap. Equations (3) and (4) are modified to:

$$C_{u\phi}(m + 1) = \frac{1}{2^M - 2^m + 1} \sum_{n=0}^{2^M - 2^m} \bar{u}_n(m) \bar{\phi}_n(m), \quad n = 1, \dots, 2^M - 2^m + 1, \quad (5)$$

with:

$$\bar{u}_n(m) = \frac{1}{2^m} \sum_{i=n}^{n+2^m-1} u r_i(m). \quad (6)$$

The non-orthogonal MRD is normalized using calculated turbulent fluxes to ensure comparability with the orthogonal MRD.

Another advantage of the non-orthogonal MRD is the possibility to extend the decomposition to more time scales m . Howell and Mahrt (1997) suggest setting $m = \log_2(2k)$, $k = 1, 2, 3, \dots, 2^{M-1}$. However, that includes many steps and, thus, the computational effort is tremendous. Therefore, we adapted the non-orthogonal MRD to be used with multiple independent series for m . Instead of only setting $m = m_1 = 1, 2, \dots, 2^M$, a non-orthogonal MRD can also be evaluated for $m_2 = 3m_1 = 3, 6, \dots, 3 \cdot 2^{M-2}$, $m_3 = 5m_1 = 5, 10, \dots, 5 \cdot 2^{M-3}$, and so on. The evaluation is truncated when the desired total number of time scales is reached.

Figure 4a shows a comparison of an orthogonal (blue) and non-orthogonal moving window (orange, dashed) MRD for a 12 h period over snow. The MRD window width is $M = 15$ corresponding to ≈ 27 min. Decomposed turbulent variables are the vertical wind speed w and the sonic temperature T_s , yielding the vertical sonic temperature flux $w'T'_s$. The shaded areas indicate the region between the 25% and the 75% quartiles. Both curves show a maximum negative flux contribution for time scales between 5 s and 10 s. At short time scales non-orthogonal MRD shows a slightly smaller flux contribution than orthogonal MRD. However, for larger time scales both MRDs agree well. Generally, a deviation between the two methods is expected due to a difference in phase and number of the averaging segments. In Fig. 4b, the non-orthogonal moving window MRD with 15 discrete time scales (orange curve in Fig. 4a) is compared to a non-orthogonal MRD using 106 time scales. It becomes obvious that an extension to more time scales does not change the shape of the cospectrum. However, it adds more detailed information on the cospectrum between the 15 discrete time scales. In summary, normalized non-orthogonal MRDs, as employed in this study, can be interpreted equivalent to “traditional” orthogonal MRDs.

We show the decomposed scales in units of time (i.e. time scale τ on the x-axis in Fig. 6). Employing Taylor’s hypothesis (Taylor 1938) and using the mean wind speed during the individual periods, τ can be converted to spatial scales.

The MRDs shown in this study are created using Julia (Bezanson et al. 2017) and Matplotlib (Hunter 2007). We use scientific, perceptually uniform colour maps from Hunter (2007) and Crameri et al. (2020).

3 Meteorological Conditions

3.1 Weather Pattern

In Fig. 5, we present the data recorded by the AWS during the campaign.

We observed an increasing air temperature trend during the 21 day observation period. High relative humidity at the beginning and towards the end of the period indicates cloudy and humid conditions. There were two major snow falls on 22 May and 23 May, each yielding ≈ 10 cm of new snow. Due to warm and sunny weather, the new snow melted within 12 h

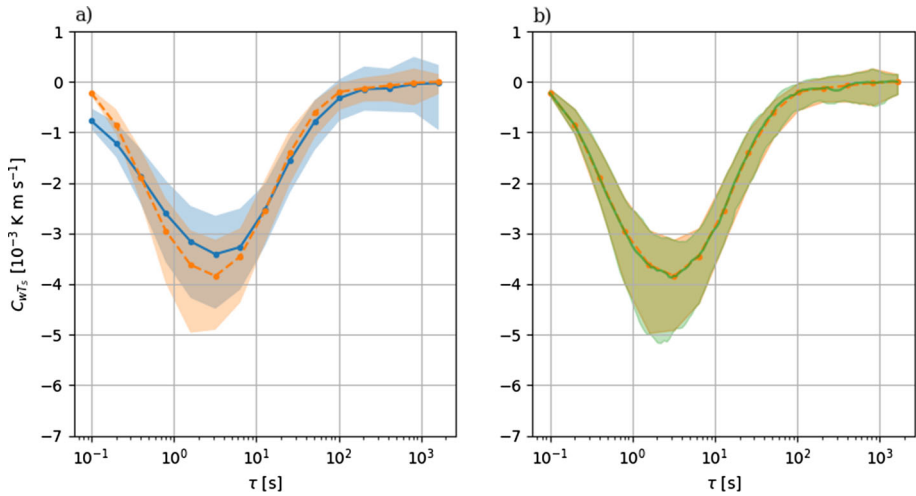


Fig. 4 **a** Comparison of an orthogonal moving window MRD (blue) and a non-orthogonal moving window MRD (orange, dashed) for a 12 h period over snow. On the x-axis, the time scale, τ , is shown, while the y-axis indicates the cospectrum $C_w T_s$. The shaded region is defined by the 25% and the 75% quartiles. **b** The non-orthogonal moving window MRD from a) (orange, 15 discrete values for τ) compared to a non-orthogonal moving window MRD using 106 discrete values for τ for the decomposition (green)

after deposition. After 5 June, there were a few minor rainfall events < 1 h with minor precipitation amounts. During the melt phase, especially on 28 May and from 30 May to 1 June, the conditions were characterized by clear skies and maximum incoming shortwave radiation. On 27 and 29 May, developing cumuli attenuated the incoming shortwave radiation already before noon. The attenuation is visible in Fig. 5c. Until 24 May we measured wind gusts up to 18 m s^{-1} . After that, only few wind gusts exceeded 10 m s^{-1} and the mean wind speed was largely below 5 m s^{-1} . In the wind direction plot, the two main wind directions appear: Up valley flow (NNW) and down valley flow (SSE). They are marked according to the corresponding wind direction class as explained in Sect. 3.2. The bottom panel shows the snow cover fraction f_s for the Dürrboden area. The strongest decrease of snow cover fraction occurred between 28 May and 5 June, when air temperatures constantly rose and the weather was mostly clear. Furthermore, during that period the weather was influenced by interrupted Föhn (see Sect. 3.2).

3.2 Flow Regimes

Due to the topography of the straight Dischma valley, two main flow directions can be distinguished. The dominance of those two flow directions is visible in the wind direction panel of Fig. 5 and the climatological flux footprints in Fig. 1. During sunny days around noon, in the absence of counteracting synoptic forcing, a thermally driven up valley flow developed (Urfer-Henneberger 1970; Whiteman and Doran 1993; Zardi and Whiteman 2013; Farina and Zardi 2023). Its onset, strength, and duration depend on the atmospheric conditions and the interplay with other flows. When the surface heating decreased in the evenings, the flow direction switched back to down valley around 1900 LT at the latest. The second main flow direction was down the valley. Down valley flow typically occurred from evening to the next morning until the up valley flow set in again. As with up valley flow, down valley flow mainly

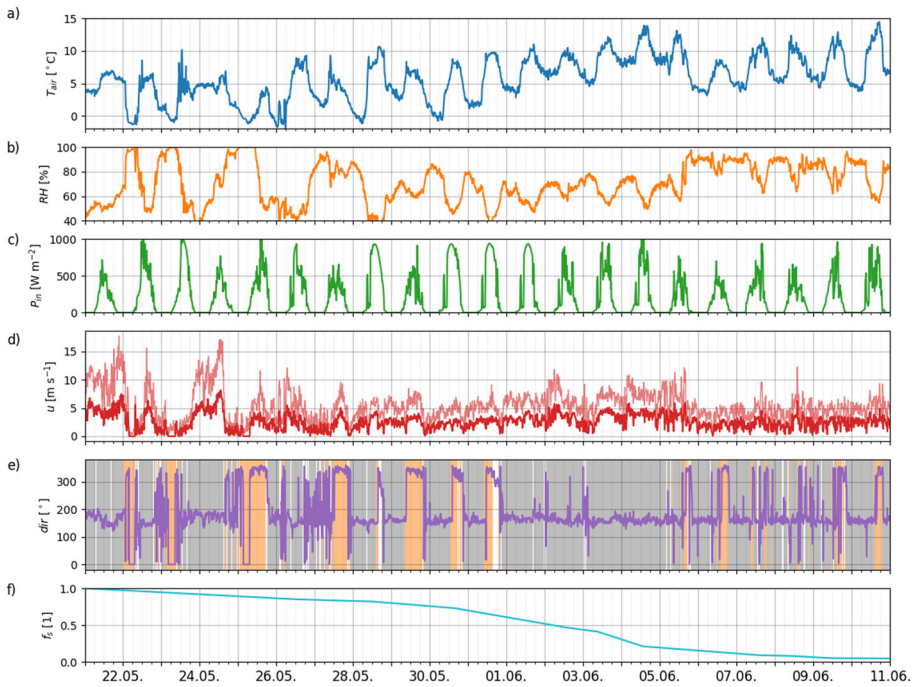


Fig. 5 Plot displays the following variables from top to bottom: **a** air temperature, T_{air} , and **b** relative humidity RH at a height of 4 m above the surface, **c** incoming shortwave radiation P_{in} , **d** wind speed measured by a propeller anemometer at a height of 3.5 m above the surface u (red: 10 min mean, light red: 10 min gusts). The background colours in the wind direction panel **e** denote the corresponding wind direction class as introduced in Sect. 3.2. **a–e** Shows data recorded by the AWS. The bottom panel **f** shows the snow cover fraction f_s evaluated from the UAV images

Table 2 Flow direction groups during the observation period

Flow group	Direction interval [°]	Occurrence(%)	Background colour in plots
Up valley	[310, 20]	19	Orange
Down valley	[130, 200]	72	Grey
Cross valley]200, 310[∪]20, 130[9	White

was thermally driven. We assume that down valley flow was enhanced by cold, continuously snow covered, and glacierized northern slopes at the back of the catchment.

Westerly winds occurred during afternoons and the calm transition from up valley to down valley flow. Those flows can be explained by heating the snow free, west facing slopes with the afternoon/evening sun. The resulting anabatic flow led to westerly winds at the bottom of the slopes at Dürrboden. The effects of the few periods of westerly flow on the flux footprints are also visible in Fig. 1. Similar cross valley flows have also been observed in an idealized modelling study by Schmidli (2013). Due to the rare occurrence of flows not aligned with the valley axis, they are combined into the “cross valley” flow group. Table 2 gives an overview of the identified flow groups, their wind direction intervals, and the frequency of occurrence.

Wind directions between 320° and 20° are denoted as up valley, and between 130° and 200° as down valley flows. All other flow directions are classified as cross valley.

Table 2 also contains the background colour used in Figs. 5, 7, 8, 9, 10, 11, 12, 13 and 14 to identify the wind direction classes. We used the propeller anemometer at the AWS at a height of 3.5 m above the surface to determine the wind direction classes for the analysis in the following sections.

Mott et al. (2017) also found two main wind directions in the Dischma valley. Using wind speed and direction criteria, they categorized data from three ablation periods into three groups: synoptic south, synoptic north, and thermally driven. Since we focus on small scale processes, the driver of the flow is of minor relevance for the analysis and hereafter we do not distinguish between thermally or synoptically driven flow.

However, a special case is Föhn. During Föhn, increased wind speeds and weaker stability enhance vertical mixing (Drobinski et al. 2007; Haid et al. 2022). At the measurement site, the wind direction during Föhn is south. Since that aligns with the direction of the katabatic flow, it is difficult to separate the two. To classify Föhn and non-Föhn events, we utilize the mixture model presented in Plavcan et al. (2014). The model yields a Föhn probability using wind speed measured at the AWS as a primary classifier. As a concomitant classifier, we chose wind direction and relative humidity measured at the AWS. Furthermore, the model uses the potential temperature difference between a ridge station close to Piz Grialetsch (see Fig. 1 for location) and the AWS as a concomitant classifier. The resulting Föhn periods relevant for further analysis are

- 21 May 0000 LT to 25 May 1800 LT, interrupted twice by different flow
- 1 June 0000 LT to 5 June 1500 LT, disrupted and superimposed by thermal and synoptic flows.

For further details we refer the reader to Online Resource 2.

4 Separation of Turbulent and Non-Turbulent Motions

To separate turbulent from non-turbulent flow, we computed MRDs for the entire observation period from 21 May to 11 June. Figure 6a displays the MRDs for the 2 m level at the ECT, while Fig. 6b shows the MRDs for the 5 m EC sensor at the AWS. The MRDs were classified into two categories: statically unstable (positive $w'T'_s$, red) and stable (negative $w'T'_s$, blue), with stable conditions comprising approximately two thirds of all periods for both sensors.

Upon comparison of the spectral structures of decompositions of both levels during stable periods, we observed similar median values for both levels for $\tau < 100$ s. At a measurement height of 2 m, the maximum cospectral contribution is observed at $\tau \approx 2$ s, while at a height of 5 m, the maximum contribution was observed at $\tau \approx 10$ s. This difference is influenced by differences in stratification and a spatial limitation of the eddy size due to the respective distance to the surface. For $\tau > 100$ s, a clear difference is apparent. While the measurement at 2 m above snow shows negligible cospectral contribution, the 5 m measurement at the AWS reveals substantial cospectral contribution for $\tau > 100$ s. The median of this submeso scale cospectrum at 5 m is positive with a wide interquartile range indicating strong variability.

We obtain a smooth distribution with large variability for the atmospherically unstable periods at the 2 m level. Similar to the decomposition of the stable periods, there is no submeso scale contribution. However, for the EC sensor at the AWS (5 m above the surface), the decomposition is more complex. Two maxima in the median of all decompositions indicate

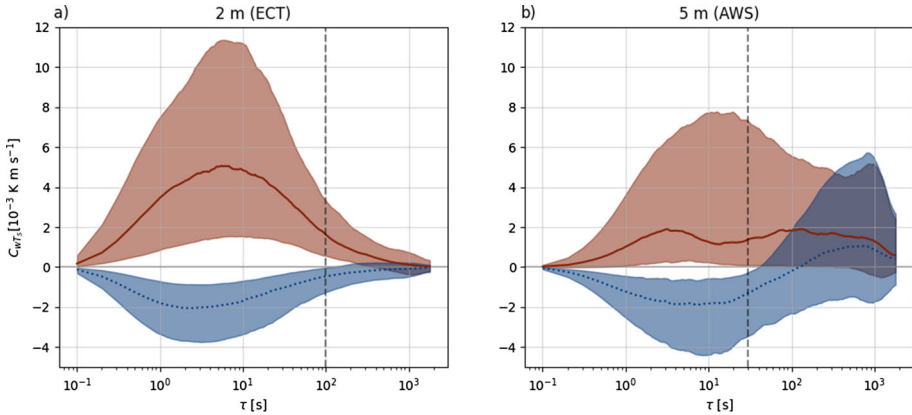


Fig. 6 **a** MRDs for the EC sensor on the ECT at the height of 2 m above the surface and **b** the EC sensor on the AWS at 5 m above the surface. Red corresponds to unstable, and dotted blue to stable conditions. The solid lines show the median and shaded areas indicate the interquartile range (25–75%). The vertical dashed lines indicate the chosen Reynolds averaging time for the corresponding instrument

a scale separation between different processes. Furthermore, there is a high variability of the cospectrum for larger scales, suggesting the presence of variable submeso scale motions.

The Reynolds averaging time separates turbulent (shorter time scales) from submeso scale motion (larger time scales) and is used to calculate turbulent fluxes. We followed the approach of Vickers and Mahrt (2003) to determine the Reynolds averaging time. They propose a cospectral gap between turbulent motion and larger, meso scale motion. Contrary to turbulence, they describe the meso scale motion as chaotic with a large spread. According to Vickers and Mahrt (2003) and Mott et al. (2020), we used as a criterion for the cospectral gap the time scale at which the upper quartile of the decomposed fluxes becomes positive. We chose a time scale of 100 s for all sensors on the ECT. As visible from Fig. 6a, larger time scales did not contribute noticeably to the total flux for both stable and unstable phases. Therefore, the obtained fluxes from the 2 m sensor at the ECT are not very sensitive to the chosen averaging time. It is challenging to define a suitable time scale for the 5 m EC sensor at the AWS. We set the averaging time as 30 s. This is a compromise between unstable and stable periods. For unstable stratification, the local minimum in the median cospectrum indicate a shorter separation time scale (≈ 20 s). During stable periods, the 75% quartile points towards a longer separation time scale (≈ 50 s). For consistency, we use 30 s for all stabilities. Similar time scales have been used in other studies (for example Mahrt and Vickers 2006). Online Resource 3 shows MRDs for all fixed sensors.

5 Evolution of Turbulence During the Melt Out

In this part, we aim to gain information on how buoyancy fluxes ($\overline{w'T'_s}$), air temperature heterogeneity represented by sonic temperature variance ($\overline{(T'_s)^2}$), and turbulence kinetic energy (e) change with a decreasing snow cover fraction. Buoyancy fluxes indicate the local stability at the sensor height. Especially the height of the SIBL can be diagnosed using the buoyancy fluxes (negative/downward fluxes within SIBL, positive/upward fluxes aloft). Furthermore, we use temperature variance as a diagnostic of the changing surface temperature heterogene-

ity on the near-surface atmosphere. The turbulence kinetic energy e provides information about the time scale of energy containing eddies. In the following, we mostly focus on local processes caused by the presence of snow and bare ground at the measurement site. Additionally, there might be influences by advection from remote sources, such as internal gravity waves.

Figure 7 shows moving-window MRDs of the three variables during the entire observation period.

The moving-window MRDs in Fig. 7b, d, and f reveal strong temporal and spectral heterogeneity throughout campaign. For the following, we separate the observation period into three periods according to characteristics in the spectral decompositions:

- Föhn: 21 to 25 May (interrupted twice) and 1 to 5 June (disturbed by other flow regimes).
- Period 1: 26 May to 1 June, *Deep SIBL*
- Period 2: 5 June to 11 June, *Strong diurnal variations in turbulence characteristics*

The periods are indicated by the bars in Fig. 7h. We discuss the periods separately in the following sections.

5.1 Föhn

Two Föhn events at the beginning of the observation period are particularly noteworthy. The high wind speeds during those events led to shear generated turbulence and, thus, peaks in the e spectrum at time scales $\mathcal{O}(100\text{ s})$. In contrast, the Föhn event from 1 June to 5 June exhibited less spectral contribution at time scales $\mathcal{O}(100\text{ s})$, which can be attributed to reduced wind speeds and less turbulence generated by shear. As warmer air impinged and partially displaced cold air adjacent to the snow surface during the second Föhn period, we also observed enhanced $(T'_s)^2$ on time scales $\mathcal{O}(100\text{ s})$. Furthermore, during these Föhn periods, we observed pronounced negative values for $\overline{w'T'_s}$ (downward), a pattern consistent with findings from previous Föhn studies (e.g. Drobinski et al. 2007; Haid et al. 2022). However, during the second Föhn period from 1 to 5 June, which was disturbed by non-Föhn periods, we measured positive daytime buoyancy fluxes starting on 2 June. The pattern of the daytime variation after 2 June in Fig. 7b resembles the days following the Föhn period. We explain the positive daytime buoyancy fluxes as follows. As visible in the UAV orthophotos in Fig. 3, more bare ground emerged south of the snow patch with the ECT. The snow cover fraction on 2 June was $f_s \approx 0.5$. As a consequence, the SIBL depth decreased below the measurement height of 2 m and we measured positive $\overline{w'T'_s}$. These observations suggest that, in case of high surface heterogeneity, the influence of the flow driver (in this instance, Föhn) on the measured turbulence quantities was subordinate. Instead, the snow cover fraction and the local distribution of patches were the dominating factors characterizing the turbulence.

5.2 Period 1: Deep Stable Internal Boundary Layer

From 26 May to 1 June, the snow cover fraction was still high. The surface was characterized by snow with, at the beginning, few isolated snow free patches. Towards the end of this period, more bare patches emerged. With the melting snow surface at 0°C , air temperatures $> 0^\circ\text{C}$, and advection of warm air from isolated bare patches, stable internal boundary layers (SIBLs) developed above snow (Garratt 1990). We measured negative $\overline{w'T'_s}$ (Fig. 7c), which indicates that the SIBLs were deep enough to include the EC sensor at 2 m.

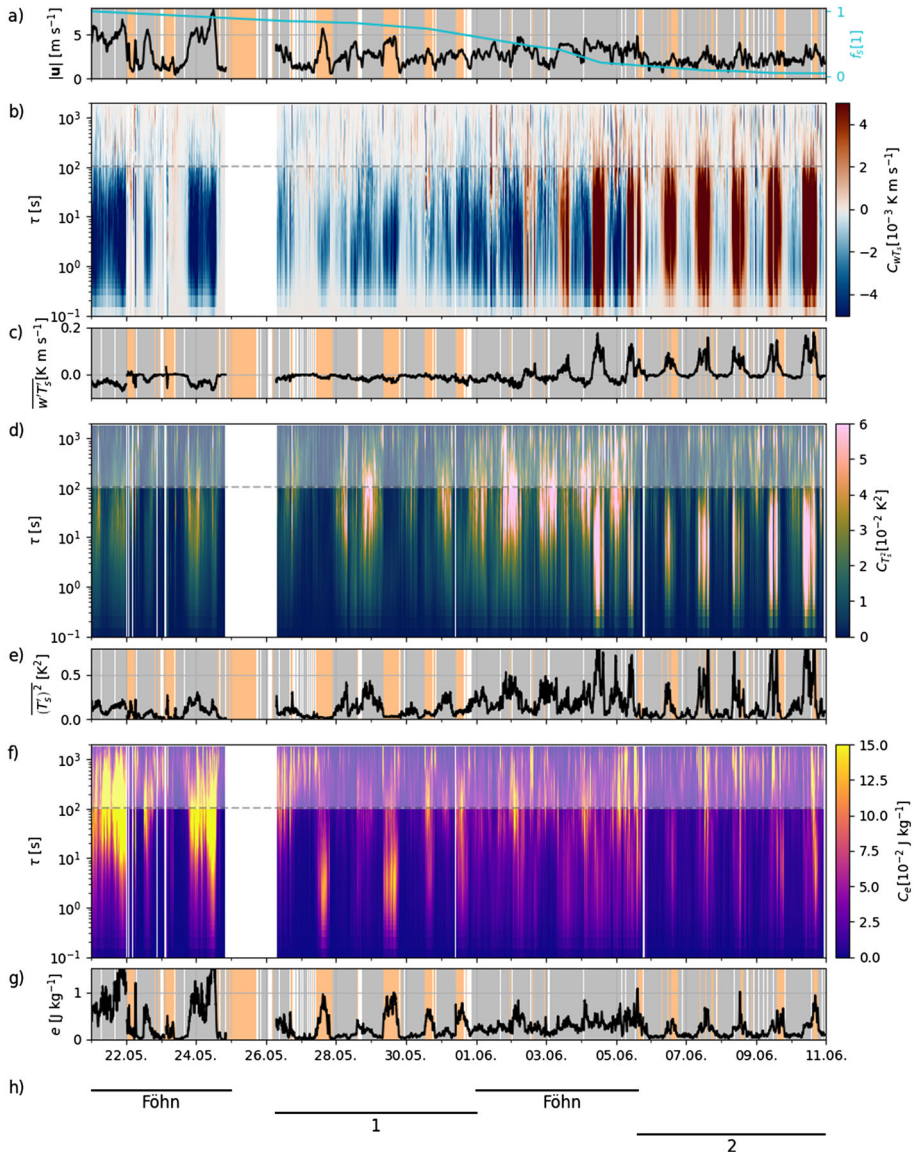


Fig. 7 Moving-window MRDs of data measured at the 2m EC sensor at the ECT. **a** The mean wind speed is plotted as a black curve on the left y-axis. The background colours indicate the wind direction class (see Sect. 3.2). Orange corresponds to up valley wind, grey to down valley flow, and white denotes wind from other directions. On the right y-axis the snow cover fraction f_s as obtained from the UAV orthophotos is shown. **b, d, e** Moving-window MRD of the buoyancy fluxes $\overline{w'T'_s}$ (b), the sonic temperature variance $(T'_s)^2$ (d), and the turbulence kinetic energy e (f). A vertical slice corresponds to a 'normal' MRD. The x-axes show the time during the observation period, while the y-axes display the time scale τ of the spectral decomposition corresponding to the x-axis in Fig. 6. The dashed horizontal lines correspond to the Reynolds averaging time (see Sect. 4), splitting turbulence (below) and larger, submeso scale motion (above). **c, e, g** Integral of the decomposed variable for turbulent motion (short time scales up to Reynolds averaging time). The gap from 24 May 1900 LT to 26 May 0700 LT is due to bad weather and a subsequent power outage. **h** indicates the periods that are separately discussed in the following

Within the SIBL, the main air temperature variances were present on scales $20 \text{ s} \leq \tau \leq 500 \text{ s}$. These variances were increased during nighttime with low wind speeds as visible in Fig. 7e, g. According to Zilitinkevich et al. (2007) the observed temperature variance in the stable near-surface atmospheric layer is a measure of the turbulence potential energy. Turbulence is suppressed by the strong stratification in the SIBL over snow and energy is transferred from turbulence kinetic energy to turbulence potential energy. This is supported by an observed decrease in e concurrent with an increase in $(T'_s)^2$. On the contrary, especially during daytime of 29 May, increased wind speeds led to shear generation of turbulence and thus weaker stability. The total turbulence energy was then mostly contained in e and $(T'_s)^2$ as a measure of turbulence potential energy, was low.

For e , two different regimes can be observed: On 27 and 29 May, we detected e on short turbulent scales $\mathcal{O}(10 \text{ s})$ similar to the late ablation period (also see Fig. 7g). On the other days in this period, we observed mostly larger scale contributions. The time scales of e were similar to the buoyancy-driven e in period 2, when the surface at the measurement site was strongly heterogeneous (see Sect. 5.3). In contrast, on 27 and 29 May, the snow cover at the measurement site was still almost continuous. Therefore, we hypothesize that the pronounced up valley winds on those days advected buoyancy-driven, short time-scale turbulence caused by surface heterogeneity further down the valley. We would expect the increased wind speeds to cause shear generated turbulence on scales $\mathcal{O}(100 \text{ s})$ similar to the first Föhn period (21 to 25 May). The factors contributing to the damping of this larger-scale e on 27 and 29 remain unclear.

5.3 Period 2: Diurnal variations

As the snow cover fraction f_s further decreased between 5 and 11 June, only few snow patches remained. They were surrounded by large areas of bare ground. We observed pronounced diurnal variations in $w'T'_s$. During nights, the radiation balance is negative, resulting in surface cooling. Therefore, typically stable conditions and negative $w'T'_s$ prevail. During the day, incoming shortwave radiation results in a positive radiation balance for bare ground and, thus heating the surface. The stability of the near-surface atmospheric layer changes towards statically unstable with more bare ground emerging. The SIBLs adjacent to the snow patches grow only to shallower heights. The lower the f_s , the shallower the SIBLs adjacent to the remaining snow patches are (Mott et al. 2017; Schlögl et al. 2018b) (also see Fig. 12 and discussion thereof). Above the SIBL, at the 2 m measurement level, we measured positive $w'T'_s$ (upward) indicating an unstable stratification. Thus, layers of different stability alternate within short lateral and vertical distance (Mott et al. 2017; Harder et al. 2017).

Especially the temperature variances show a clear scale transition starting on 4 June. The unstable stratification (TPE not defined, because Brunt–Väisälä frequency becomes imaginary) indicated by positive $w'T'_s$, points to the fact that temperature variances need to be interpreted differently. The need for a different interpretation is further indicated by a change in the interplay between temperature variance and turbulence kinetic energy. Earlier, in period 1, temperature variance and turbulence kinetic energy showed alternating peaks: When we measured high $(T'_s)^2$, concurrently e was low, and vice versa. After 4 June, during daytime, both variables peaked simultaneously on turbulent time scales ($2 \text{ s} < \tau < 50 \text{ s}$). We argue that, after 4 June, peaking temperature variance and turbulence kinetic energy reflected the intermittent advection of warm air from bare ground over the snow surface.

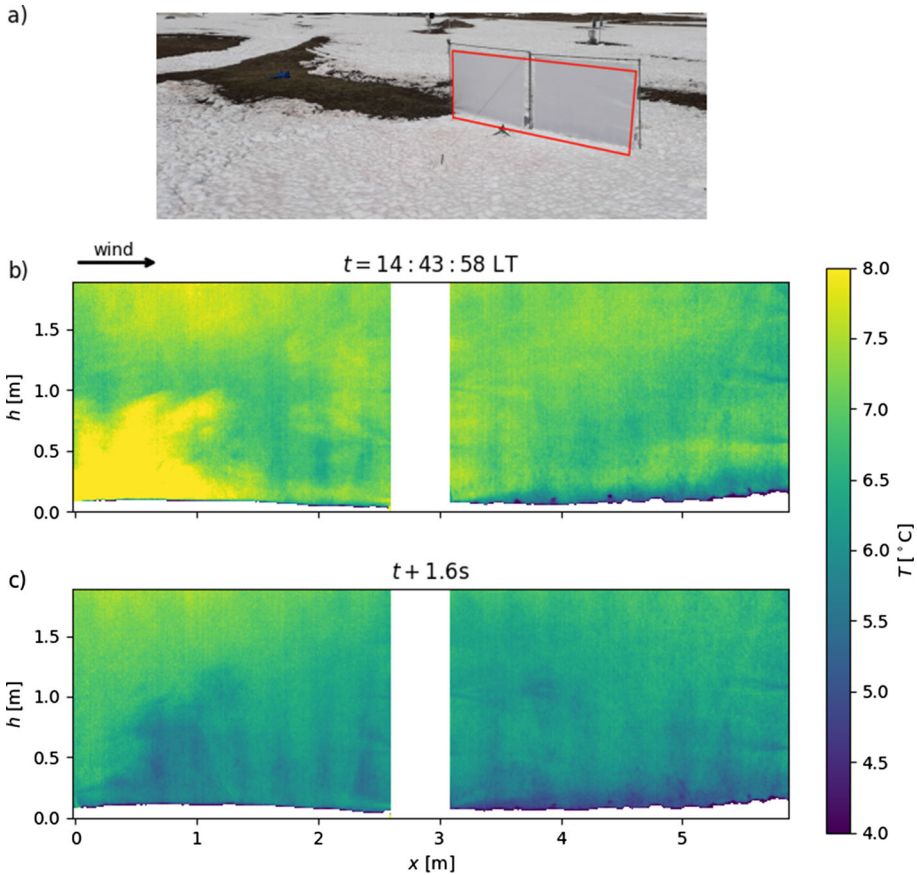


Fig. 8 Measurements with the screen setup visualizing the temporal dynamics of the atmospheric layer adjacent to the surface. **a** Overview of the set-up. The red box shows the excerpt of the following panels. **b** The thermal infrared snapshot visualizes the near-surface advection of warm air. The x-axis shows the downwind distance from the transition from bare to snow (transition at $x = 0$ m). The y-axis denotes the height above the bottom of the frame. The up valley flow blows from left to right as indicated by the arrow. **c** Only 1.6 s later the near-surface atmosphere is a few degrees colder and the warm air plume is not visible anymore

In order to facilitate the visualization of this highly dynamic near-surface layer processes, we deployed thin synthetic screens vertically across the transition from bare ground to snow (Haugeneder et al. 2023). The temperature of the screens, captured by a thermal infrared camera, serves as a proxy for the local air temperature. For a more thorough understanding of the following results, we strongly encourage the reader to watch the real time video in Online Resource 4.

The snapshot in Fig. 8b visualizes the intermittent advection of a plume of warm air over snow. The plume only affects the atmosphere's lowest ≈ 1 m at the transition from bare to snow. Aloft and further down wind, colder air is still present. Only 1.6 s later, in the snapshot in Fig. 8c, the plume disappeared and the air adjacent to the surface is significantly colder. The strong temporal dynamics reflect the interplay between warm air advected from over bare ground and the cold air adjacent to the snow surface.

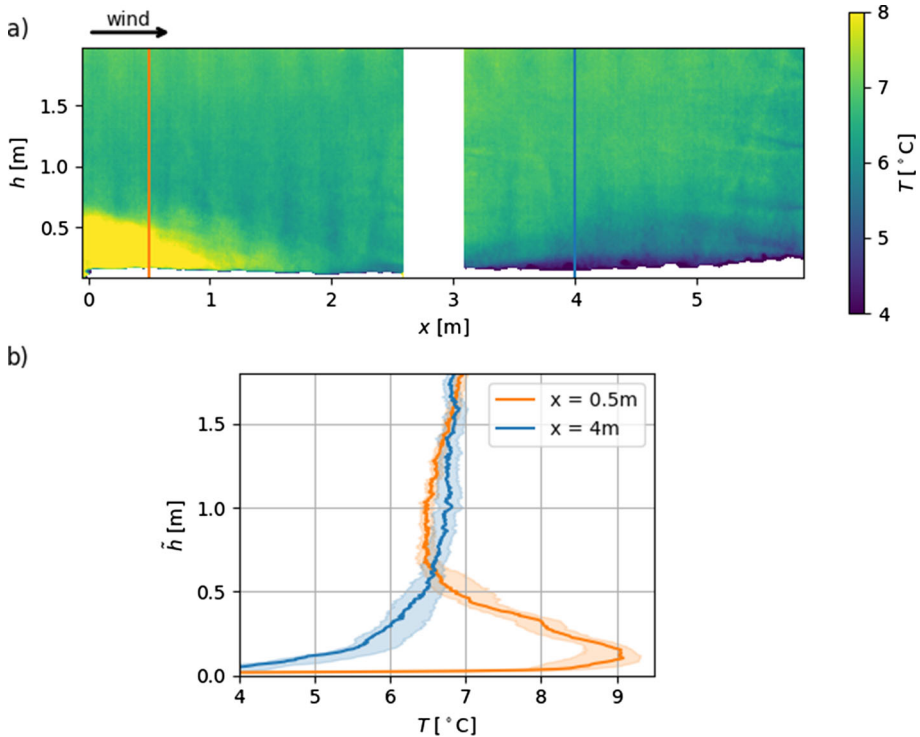


Fig. 9 **a** Similar figure set-up as in Fig. 8b, c. The data are temporally averaged over 1 s. The two vertical lines indicate the location of vertical temperature profiles as shown in **b**. On the y-axis of **b** the height above the snow surface \tilde{h} is plotted. The profiles are averaged over a 20 cm wide column and 1 s. The shaded regions indicate the 25–75% interquartile range

The strong spatial heterogeneity is evident in both parts of Fig. 9. Within a lateral distance of 3.5 m the air temperatures at 0.2 m above the snow surface differed by 3.5 °C due to the intermittent advection of a shallow plume of warm air at the upwind edge of the snow patch. The advection only affected the lowest layer adjacent to the snow surface. It led to a strongly stable stratification within the SIBL. The warm air close to the surface presumably also increased negative buoyancy fluxes and, thus, surface energy input close to the snow at the leading edge. Previous studies have measured the resulting influence of the so-called leading edge effect on the melt rates (Mott et al. 2011, 2018; Schlögl et al. 2018a). Above a height of $\tilde{h} \approx 0.7$ m the atmospheric layer during the snapshot shown in Fig. 9b was mixed and there were only minor differences in stratification.

5.4 Comparison: High Versus Low Snow Cover Fraction

The difference of the turbulence structure with high and low f_s is further elucidated in Fig. 10. In the first period (left column), f_s decreased from 0.80 to 0.70, while in the second period (right column), f_s ranged from 0.19–0.12. Figure 10b shows that negative buoyancy fluxes prevailed in the first period. During daytime, pronounced negative fluxes were caused by increased wind speeds (Fig. 10a) and resulting shear driven turbulence. The SIBL was deeper than 2 m, including the EC sensor. Conversely, during the second period, we measured

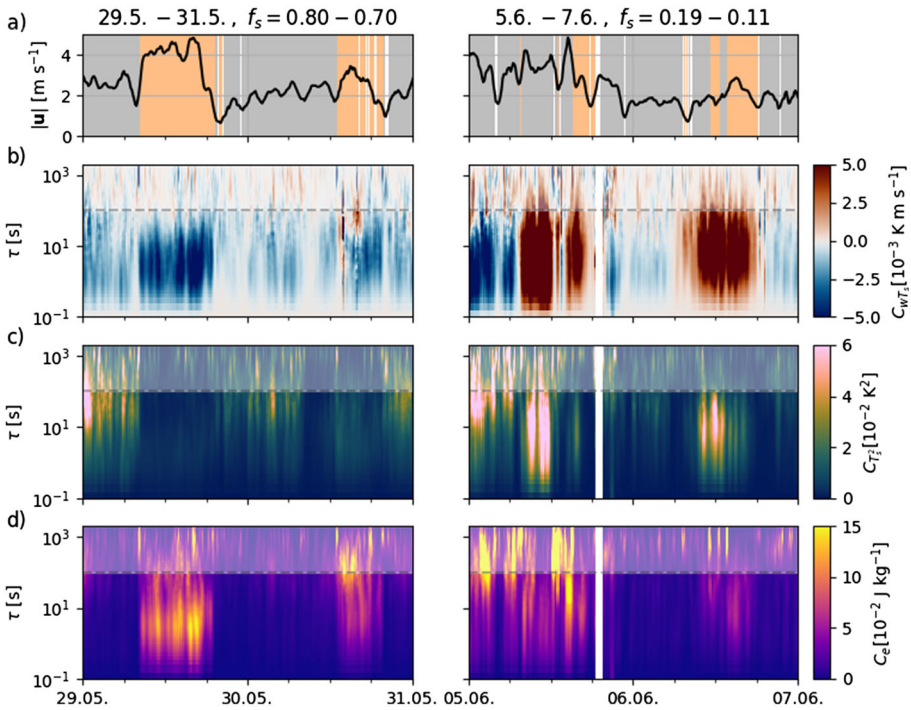


Fig. 10 Spectral decompositions for two 2 d periods. In the left column data from 29 to 31 May, and in the right column from 5 to 7 June are shown. Furthermore, the range of snow cover fractions f_s is given. In row **a** the wind speed is plotted with background colours indicating the wind direction class. In the following rows, spectral decompositions of buoyancy fluxes $\overline{w'T'_s}$ (**b**), sonic temperature variance $\overline{(T'_s)^2}$ (**c**), and turbulent kinetic energy e (**d**) are depicted. All data are calculated from the EC measurements at 2 m at the ECT

positive $\overline{w'T'_s}$ on turbulent time scales. These positive fluxes indicate a SIBL depth < 2 m. Above the SIBL, at the height of the EC sensor unstable stratification prevailed.

The left column of Fig. 10c, d illustrate the conversion between turbulence potential energy and turbulence kinetic energy. The cold snow surface and calm winds during nighttime lead to a strongly stable stratification. Then, increased $\overline{(T'_s)^2}$ and concurrently almost zero e indicate the substantial mitigation of turbulence and the conversion of e into turbulence potential energy. While increased wind speeds and weaker stratification during daytime favour turbulent energy being contained in turbulence kinetic energy. The increased wind speeds and weaker stratification on 29 May led to less dampened vertical motion and thus more small scale e compared to 30 May. During the second period, daytime increased $\overline{(T'_s)^2}$ on shorter, turbulence time scales are in line with the observed intermittent advection of warm air (see Figs. 8, 9).

5.5 Vertical Profiles of Turbulence

The following part aims at examining turbulence at various measurement heights, mainly at the ECT above snow at the transition from bare ground to snow covered surface (c.f. Figure 1 for the position of the ECT). The 5 m measurement was taken at the AWS, while

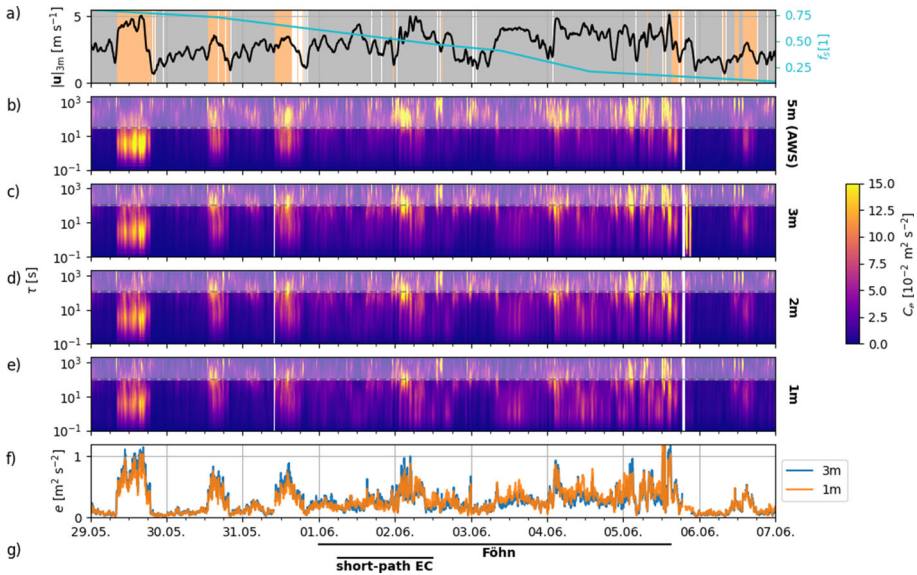


Fig. 11 Decomposition of e at various measurement heights for 29 May–7 June. **a** Horizontal wind speed measured at 3 m above the surface on the left y-axis. The background colors indicate the wind direction class. Additionally, we show snow cover fraction f_s on the right y-axis. **b** shows data for the 5 m EC sensor at the AWS. The panels **c–e** refer to data measured by instruments at the ECT. The height is indicated on the right. We compare e for 3 m and 1 m measurements in panel **f**. **g** visualizes the Föhn period as identified at the beginning of Sect. 5. Furthermore, we show the period with the short-path EC sensor presented in Figs. 13 and 14

the other three stem from data recorded by sensors at the ECT. Figures 11 and 12 display decompositions of e and $\overline{w'T'_s}$ at different measurement heights.

The decompositions of e show a similar spectral pattern throughout all heights at the same measurement time, with both smaller scale turbulence $\mathcal{O}(10\text{ s})$ and larger scale motions observed in data at all sensor heights simultaneously. Furthermore, the magnitude of e was very similar, as shown for data from 3 m above snow compared to 1 m in Fig. 11f. Homogeneous turbulence pattern with height are also confirmed by the $\overline{w'T'_s}$ decompositions in Fig. 12b–e before 1 June and after 5 June. Turbulent buoyancy flux spectra showed similar pattern throughout the measurement heights with few exceptions in the 5 m measurement. This homogeneous turbulence (and larger scale motion) pattern with height observed in both decomposition profiles indicates sufficient mixing. Disturbances were coherent, so measurements at all levels were coupled.

The three sensors at the ECT presented in Fig. 12c–e exhibited weak spectral contributions beyond the turbulent scale. The majority of the $\overline{w'T'_s}$ spectrum stemmed from short turbulent scales. In contrast, the data at 5 m (Fig. 12b) showed substantial contributions from larger scales. These differences are consistent with the clearly larger footprints of the 5 m measurement compared to the lower sensors, as shown in Fig. 1. The lack of larger scale contributions for the 2 m measurement and the difference to the 5 m data are also represented by the tails (at longer time scales) of the MRDs in Fig. 6.

In the transition period 1 to 5 June, when the snow cover fraction strongly decreased from $f_s \approx 0.6$ to $f_s \approx 0.2$ differences between measurement levels in the $\overline{w'T'_s}$ decomposition became apparent. For example, around midday on 3 June, we measured positive $\overline{w'T'_s}$ at

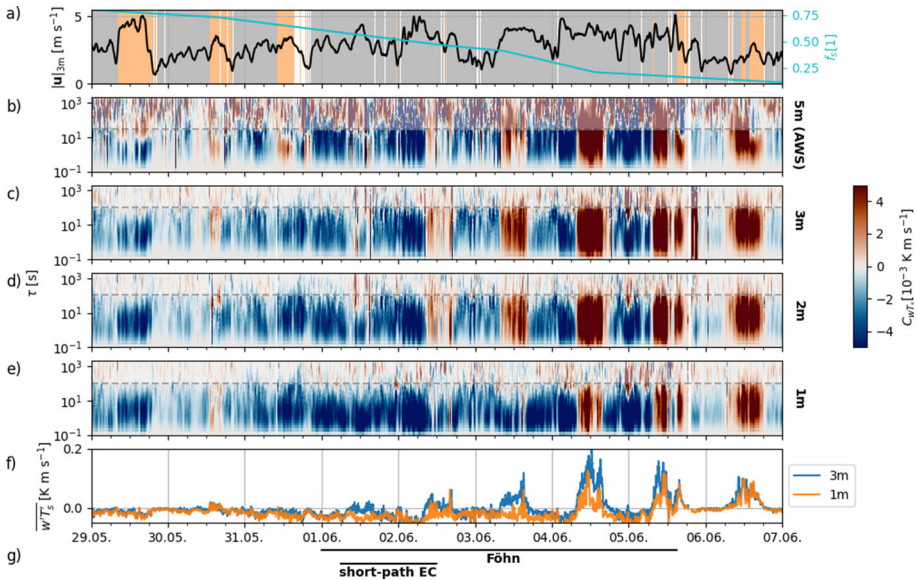


Fig. 12 Decomposition of $\overline{w'T'_s}$ at various measurement heights for 29 May–7 June. Similar figure set-up as Fig. 11. Horizontal wind speed measured at 3 m above the surface on the left y-axis. The background colors indicate the wind direction class. Additionally, we show snow cover fraction f_s on the right y-axis. **b** shows data for the 5 m EC sensor at the AWS. The panels **c**, **d**, and **e** refer to data measured by instruments at the ECT. The height is indicated on the right. We compare e for 3 m and 1 m measurements in panel **f**. **g** visualizes the Föhn period as identified at the beginning of Sect. 5. Furthermore, we show the period with the short-path EC sensor presented in Figs. 13 and 14

2 m and negative $\overline{w'T'_s}$ at 1 m. These differences can be explained by the decreasing SIBL depth. As mentioned earlier, the upper SIBL boundary is defined by a change in stability and, thus, a change in sign of the buoyancy fluxes (positive above and negative below SIBL height). Figure 12c–e show that on 2 and 3 June, positive buoyancy fluxes were observed for the upper measurement levels, while the 1 m still recorded negative fluxes within the SIBL. Therefore, the SIBL depth was between 1 m and 2 m. From 4 June on, we also measured positive buoyancy fluxes at the 1 m level. The SIBL depth decreased below 1 m. After 5 June, the SIBL is so shallow that all measurement levels are above the SIBL and, thus, are coupled again similar to the earlier period. In contrast to the stable stratification within the SIBL before 1 June, positive buoyancy fluxes indicate an unstable stratification for 6 June.

The dynamics of the SIBL depth are governed by the decreasing snow cover fraction and the resulting increased emergence of bare ground. However, the snow cover fraction as an averaged scalar descriptor of the snow coverage of the (larger surrounding) area is not the only relevant driver. Additionally, the local distribution of patches in the footprint of the EC sensors is important. For example, a longer upwind bare patch leads to warmer air being advected over the snow surface. Consequently, the negative (downward) buoyancy fluxes near the snow surface increase. In the present study, we focus on the turbulence properties above the snow patch and therefore do not take the upwind distribution of patches into account.

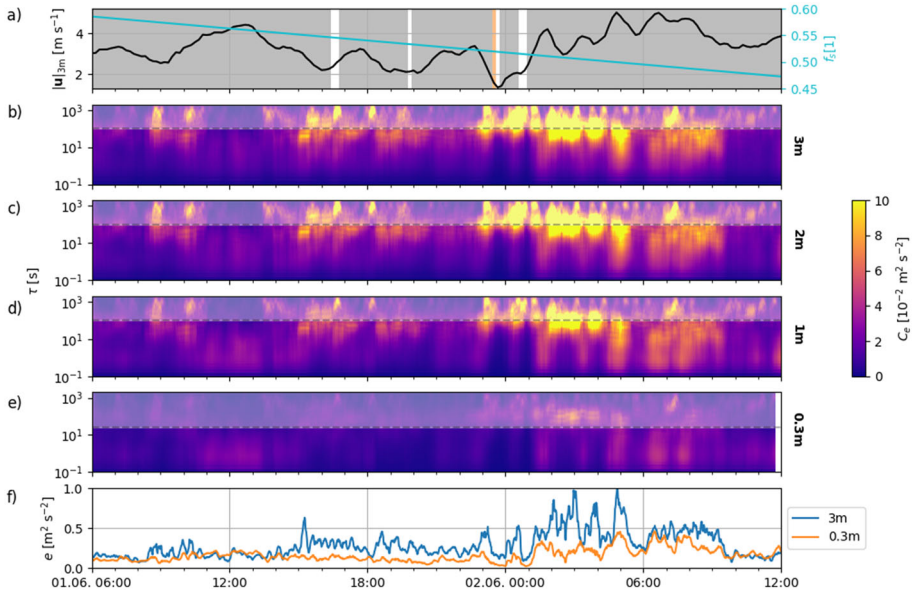


Fig. 13 Decomposition of e at various measurement heights for a 30h period when the short-path ultrasonic anemometer was installed below the instruments at the ECT. **a** Horizontal wind speed measured at 3 m above the surface on the left y-axis. The background colors indicate the wind direction class. Additionally, we show snow cover fraction f_s on the right y-axis. **b–d** show data measured by instruments at the ECT. **e** refers to data measured by the short-path ultrasonic sensor. The height of all instruments is indicated on the right. We compare e for 3 m and 0.3 m measurements in panel **f**

5.6 Near-Surface Eddy Covariance Measurements

In order to further investigate the processes close to the surface, we deployed a short-path EC sensor at the height of 0.3 m below the sensors of the ECT for a 30h period. The period is indicated in Figs. 11g and 12g. Figures 13 and 14 show decompositions of e and $(T'_s)^2$ including the 0.3 m data.

Figures 13b–e indicate that the spectral pattern of e from aloft (3 m, 2 m, and 1 m) was also present close to the surface (0.3 m). Mostly, the spectral magnitude was reduced towards the surface (c.f. Fig. 13f). Additional to the physical limitation of eddy sizes due to the height above the surface, this reduction was probably caused by the strongly stable near-surface stratification over snow. The strongly stable layer adjacent to the surface is also visible in the temperature profiles captured with the thermal IR camera in Fig. 9b. However, around midday (1 June 1000 LT–1500 LT and 2 June 1000 LT–1200 LT), e close to the surface (0.3 m and 1 m) was nearly as high as at 3 m. During those noon and afternoon times, also the sonic temperature variance at 0.3 m shown in Fig. 14e, f was increased. The increase in both variables mainly stemmed from scales $\tau \leq 10$ s. In contrast, the short scale contributions in the $(T'_s)^2$ decompositions at the upper measurement levels (3 m, 2 m, and 1 m shown in Fig. 14b–d) were strongly mitigated and hardly recognisable. The upper spectra mostly matched indicating vertical homogeneity above 1 m.

These observations point to a local near-surface process that lead to increased turbulence kinetic energy and sonic temperature variance close to the surface during daytime. As mentioned earlier and visible in the snapshots in Fig. 8b the driver was the intermittent advection

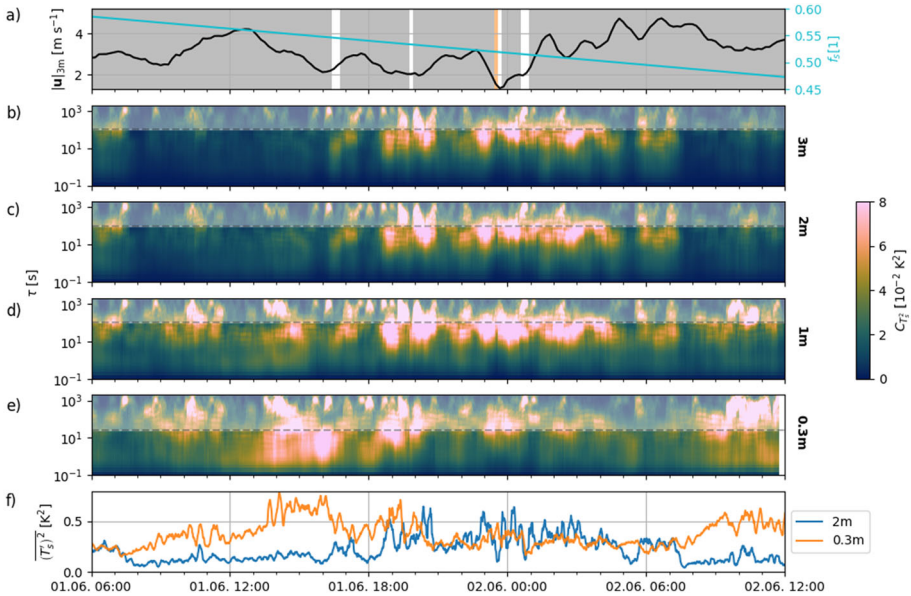


Fig. 14 Decomposition of $(T'_s)^2$ at various measurement heights for a 30 h period when the short-path ultrasonic anemometer was installed below the instruments at the ECT. Similar figure set-up as Fig. 13. **a** Horizontal wind speed measured at 3 m above the surface on the left y-axis. The background colors indicate the wind direction class. Additionally, we show snow cover fraction f_s on the right y-axis. **b**, **c**, and **d** show data measured by instruments at the ECT. **e** refers to data measured by the short-path ultrasonic sensor. The height of all instruments is indicated on the right. We compare $(T'_s)^2$ for 3 m and 0.3 m measurements in panel **f**

of warm air. Around midday, solar radiation heated the bare patches up wind of the ECT and the short-path EC sensor. The dynamic interplay between cold air adjacent to the melting snow surface and the intermittent plumes of warm air from bare ground caused the increase in $(T'_s)^2$ and *e*. At the leading edge of the snow patch (or over the total snow patch, if the snow patch is small) the advected plumes stayed close enough to the ground to only influence the lowest measurement level.

6 Conclusion and Outlook

During a snow ablation season, we conducted a comprehensive field campaign in an alpine catchment with a particular focus on characterizing the near-surface atmospheric layer over patchy snow. Our primary objective was to collect eddy covariance data at various measurement levels above the snow, aiming to provide a comprehensive understanding of the dynamics involved. To highlight the different time scales, we investigated spectra of the vertical virtual temperature flux and the turbulence kinetic energy. Analysing the evolution of the spectra over the observation time allowed us to explore the dependency of the findings on meteorological conditions and snow cover fraction. We summarize the results in Fig. 15, which displays four distinct periods: The initial Föhn phase with a continuous snow cover (a), advection of warm air from a few bare patches over snow (b), the second Föhn phase

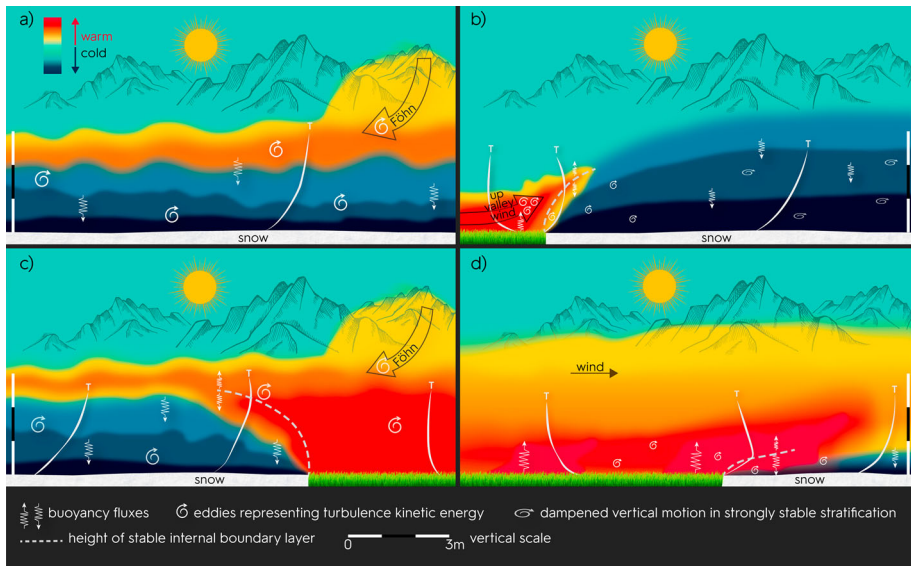


Fig. 15 The key phases observed during the campaign: **a** Föhn flow over still continuous snow cover. Intense Föhn flow prevailed over the initially continuous snow cover. The resulting high wind speeds induced shear-generated turbulence kinetic energy, accompanied by pronounced negative buoyancy fluxes. **b** Emergence of bare patches and warm air advection: As the first bare patches emerged, warm air was advected over the advancing leading edge of the snow patch by up valley winds. Calm phases exhibited strongly stable stratification, suppressing vertical motion, as indicated by the flat and faint eddies on the right side. Turbulence energy was predominantly contained in turbulence potential energy during these periods. **c**, Impingement of warm Föhn air: The high wind speeds induced shear-generated turbulence kinetic energy. **d** Intermittent advection over remaining snow patches: As only a few snow patches remained, the near-surface air above bare ground experienced significant heating. This led to intermittent advection of warm air plumes over the snow surface, forming a very shallow Stable Internal Boundary Layer (SIBL)

over patchy snow (c), and the final period with intermittent advection of warm air plumes over the remaining isolated snow patches (d).

The main findings are summarized in the following points.

- During the Föhn periods, we observed pronounced turbulence kinetic energy at scales $\mathcal{O}(100\text{ s})$. The shear-generated turbulence is indicated by large eddies and wavy transitions in temperature in Fig. 15a, c. Additionally, we observed pronounced negative buoyancy fluxes.
- In the early period of snow ablation (Fig. 15b), we recorded negative buoyancy fluxes at all measurement levels (1 m, 2 m, 3 m, and 5 m). Later, we measured negative fluxes only at 1 m, while above positive fluxes prevailed during daytime as indicated in Fig. 15d. This suggests that the SIBL above the snow patch became shallower as the snow cover fraction decreased over time.
- On 27 and 29 May, we measured turbulence kinetic energy on turbulent time scales, while on other days in this period, larger scales were present. We hypothesize that the up valley wind advected buoyancy-driven small-scale turbulence as indicated by the small eddies in the left part of Fig. 15b.
- The sonic temperature variance showed a transition in time scales as the snow cover diminished. Initially, we found the main spectral contribution to be $\mathcal{O}(100\text{ s})$ with concurrently low turbulence kinetic energy. As the SIBL depth decreased below the measurement

levels, the spectra indicate a shift towards smaller time scales \mathcal{O} (10 s), while we simultaneously observed an increase in turbulence kinetic energy (small eddies in Fig. 15d). We argue that these variances reflect the conversion of turbulence kinetic energy into turbulence potential energy in the strongly stable stratification within the SIBL during the initial period. The very weak turbulence kinetic energy in the strongly stable stratification with dampened vertical motion is indicated by the flat faded eddies in the right part of Fig. 15b. Later, with a low snow cover fraction, the variances result from the surface temperature heterogeneity in the immediate vicinity of the remaining snow patch.

- We found a mostly homogeneous pattern of turbulence with height for the measurements at 1 m, 2 m, and 3 m. An exception is when the SIBL depth is within this range, resulting in a sign change of the buoyancy fluxes.
- With strong surface temperature heterogeneity between bare ground and the melting snow, we observed intermittent advection of warm air over the snow (Fig. 15d). The plumes of warm air were shallow only affecting the lowest measurement levels up to 1 m.

To generalize the findings, additional data from different campaigns are necessary to cover multiple seasons, different locations, and various meteorological conditions. Furthermore, measurements over melting ice can help to transfer the described findings to the near-surface atmosphere over glaciers and gain information on summer-time glacier–atmosphere interaction and its consequences on summer-time glacier mass loss. The resulting knowledge will enable us to improve parameterizations of lateral heat advection in coupled hectometre-scale surface–atmosphere models. These models can investigate the accumulated effect over catchments and entire seasons.

Supplementary Information The online version contains supplementary material available at <https://doi.org/10.1007/s10546-023-00856-4>.

Acknowledgements This work is funded by the Swiss National Science Foundation (SNF) project ‘Snow–atmosphere interactions in mountains: Assessing wind-driven coupling processes and snow–albedo–temperature feedbacks’ (nr. 188554). Furthermore, our gratitude goes to Larissa Schädler for recording UAV orthophotos and assisting during the field campaign. We thank Julia Mott (nuance media) for preparing the summarizing figure. The work of Ivana Stiperski has been funded from the European Research Council (ERC) under the European Union’s Horizon 2020 research and innovation program (Grant agreement No. 101001691).

Author Contributions MH collected the experimental data and analyzed them with support and under guidance of RM, ML, IS, and DR. MH prepared a draft of the manuscript. The manuscript was sufficiently improved and complemented by feedback and ideas from RM, ML, IS, and DR.

Funding Open Access funding provided by Lib4RI - Library for the Research Institutes within the ETH Domain: Eawag, Empa, PSI & WSL.

Data and Code Availability Data is available at <https://doi.org/10.16904/envidat.399>. Documented source code can found at <https://github.com/michhau/turbpatchsno>.

Declarations

Conflict of interest The authors declare that the research was conducted in the absence of any commercial or financial relationships that could be construed as a potential conflict of interest.

Open Access This article is licensed under a Creative Commons Attribution 4.0 International License, which permits use, sharing, adaptation, distribution and reproduction in any medium or format, as long as you give appropriate credit to the original author(s) and the source, provide a link to the Creative Commons licence, and indicate if changes were made. The images or other third party material in this article are included in the

article's Creative Commons licence, unless indicated otherwise in a credit line to the material. If material is not included in the article's Creative Commons licence and your intended use is not permitted by statutory regulation or exceeds the permitted use, you will need to obtain permission directly from the copyright holder. To view a copy of this licence, visit <http://creativecommons.org/licenses/by/4.0/>.

References

- Bavay M, Lehning M, Jonas T, Löwe H (2009) Simulations of future snow cover and discharge in alpine headwater catchments. *Hydrol Proc* 23:95–108
- Bezanson J, Edelman A, Karpinski S, Shah VB (2017) Julia: a fresh approach to numerical computing. *SIAM Rev* 59:65–98
- Brauchli T, Trujillo E, Huwald H, Lehning M (2017) Influence of slope-scale snowmelt on catchment response simulated with the 3d model. *Water Resour Res* 53:10,723–10,739
- Carletti F, Michel A, Casale F, Burri A, Bocchiola D, Bavay M, Lehning M (2022) A comparison of hydrological models with different level of complexity in alpine regions in the context of climate change. *Hydrol Earth Syst Sci* 26:3447–3475
- Cramer F, Shephard GE, Heron PJ (2020) The misuse of colour in science communication. *Nat Commun* 11:5444
- Drobinski P, Steinacker R, Richner H, Baumann-Stanzer K, Beffrey G, Benech B, Berger H, Chimani B, Dabas A, Dorninger M, Dürr B, Flamant C, Frioud M, Furger M, Gröhn I, Gubser S, Gutermann T, Häberli C, Hällner-Scharnhost E, Jaubert G, Lothorn M, Mitev V, Pechinger U, Piringer M, Ratheiser M, Ruffieux D, Seiz G, Spatzierer M, Tschannett S, Vogt S, Werner R, Zängl G (2007) Föhn in the rhine valley during map: A review of its multiscale dynamics in complex valley geometry. *Q J R Meteorol Soc* 133:897–916
- Eker R, Bühler Y, Schlögl S, Stoffel A, Aydin A (2019) Monitoring of snow cover ablation using very high spatial resolution remote sens datasets. *Remote Sens* 11:699
- Farina S, Zardi D (2023) Understanding thermally driven slope winds: Recent advances and open questions. *Boundary-Layer Meteorol*. <https://doi.org/10.1007/s10546-023-00821-1>
- Fujita K, Hiyama K, Iida H, Ageta Y (2010) Self-regulated fluctuations in the ablation of a snow patch over four decades. *Water Resour Res* 46:W11541
- Garratt JR (1990) The internal boundary layer—a review. *Boundary-Layer Meteorol* 50:171–203
- Gerber F, Mott R, Lehning M (2019) The importance of near-surface winter precipitation processes in complex alpine terrain. *J Hydrometeorol* 20:177–196
- Goger B, Stiperski I, Nicholson L, Sauter T (2022) Large-eddy simulations of the atmospheric boundary layer over an alpine glacier: impact of synoptic flow direction and governing processes. *Q J R Meteorol Soc* 148:1319–1343
- Granger RJ, Essery R, Pomeroy JW (2006) Boundary-layer growth over snow and soil patches: field observations. *Hydrol Proc* 20:943–951
- Haid M, Gohm A, Umek L, Ward HC, Rotach MW (2022) Cold-air pool processes in the inn valley during föhn: a comparison of four cases during the piano campaign. *Boundary-Layer Meteorol* 182:335–362
- Harder P, Pomeroy JW, Helgason W (2017) Local-scale advection of sensible and latent heat during snowmelt. *Geophys Res Lett* 44:9769–9777
- Haugeneder M, Lehning M, Reynolds D, Jonas T, Mott R (2023) A novel method to quantify near-surface boundary-layer dynamics at ultra-high spatio-temporal resolution. *Boundary-Layer Meteorol* 186:177–197
- Howell JF, Mahrt L (1997) Multiresolution flux decomposition. *Boundary-Layer Meteorol* 83:117–137
- Hunter JD (2007) Matplotlib: a 2D graphics environment. *Comput Sci Eng* 9:90–95
- Jackson PL, Mayr G, Vosper S (2013) Dynamically-driven winds. In: Chow FK, Wekker SFD, Snyder BJ (eds) *Mountain Weather Research and Forecasting*. Springer, Dordrecht, pp 121–218
- Jansing L, Papritz L, Dürr B, Gerstgrasser D, Sprenger M (2022) Classification of alpine south Föhn based on 5 years of kilometre-scale analysis data. *Weather Clim Dyn* 3:1113–1138
- Kljun N, Calanca P, Rotach MW, Schmid HP (2015) A simple two-dimensional parameterisation for flux footprint prediction (FFP). *Geosci Model Dev* 8:3695–3713
- Kolmogorov AN (1941) The local structure of turbulence in incompressible viscous fluid for very large Reynolds numbers. *Doklady Akademii Nauk SSSR* 30:301–304
- Lehner M, Rotach M (2018) Current challenges in understanding and predicting transport and exchange in the atmosphere over mountainous terrain. *Atmosphere* 9:276
- Lehning M, Völksch I, Gustafsson D, Nguyen TA, Stähli M, Zappa M (2006) ALPINE3D: a detailed model of mountain surface processes and its application to snow hydrology. *Hydrol Proc* 20:2111–2128

- Mahrt L (2014) Stably stratified atmospheric boundary layers. *Annu Rev Fluid Mech* 46:23–45
- Mahrt L, Vickers D (2006) Extremely weak mixing in stable conditions. *Boundary-Layer Meteorol* 119:19–39
- Mott R, Egli L, Grünewald T, Dawes N, Manes C, Bavay M, Lehning M (2011) Micrometeorological processes driving snow ablation in an alpine catchment. *Cryosphere* 5:1083–1098
- Mott R, Gromke C, Grünewald T, Lehning M (2013) Relative importance of advective heat transport and boundary layer decoupling in the melt dynamics of a patchy snow cover. *Adv Water Resour* 55:88–97
- Mott R, Schlögl S, Dirks L, Lehning M (2017) Impact of extreme land surface heterogeneity on micrometeorology over spring snow cover. *J Hydrometeorol* 18:2705–2722
- Mott R, Vionnet V, Grünewald T (2018) The seasonal snow cover dynamics: Review on wind-driven coupling processes. *Front Earth Sci* 6:197
- Mott R, Stiperski I, Nicholson L (2020) Spatio-temporal flow variations driving heat exchange processes at a mountain glacier. *Cryosphere* 14:4699–4718
- Nadeau DF, Pardyjak ER, Higgins CW, Parlange MB (2013) Similarity scaling over a steep alpine slope. *Boundary-Layer Meteorol* 147:401–419
- Plavcan D, Mayr GJ, Zeileis A (2014) Automatic and probabilistic Foehn diagnosis with a statistical mixture model. *J Appl Meteorol Climatol* 53:652–659. <https://doi.org/10.1175/JAMC-D-13-0267.1>
- Pohl S, Marsh P, Liston GE (2006) Spatial-temporal variability in turbulent fluxes during spring snowmelt. *Arctic Antarctic Alpine Res* 38(1):136–146
- Reynolds D, Gutman E, Kruyt B, Haugeneder M, Jonas T, Gerber F, Lehning M, Mott R (2023) The high-resolution intermediate complexity atmospheric research (HICAR v1.0) model enables fast dynamic downscaling to the hectometer scale. *Geosci Model Dev Discussions* 1–30
- Rotach MW, Gohm A, Lang MN, Leukauf D, Stiperski I, Wagner JS (2015) On the vertical exchange of heat, mass, and momentum over complex, mountainous terrain. *Front Earth Sci* 3:1–14
- Schlögl S, Lehning M, Nishimura K, Huwald H, Cullen NJ, Mott R (2017) How do stability corrections perform in the stable boundary layer over snow? *Boundary-Layer Meteorol* 165:161–180
- Schlögl S, Lehning M, Mott R (2018a) How are turbulent sensible heat fluxes and snow melt rates affected by a changing snow cover fraction? *Front Earth Sci* 6:154
- Schlögl S, Lehning M, Fierz C, Mott R (2018b) Representation of horizontal transport processes in snowmelt modeling by applying a footprint approach. *Front Earth Sci* 6:120
- Schmidli J (2013) Daytime heat transfer processes over mountainous terrain. *J Atmos Sci* 70:4041–4066
- Schotanus P, Nieuwstadt F, Bruin HD (1983) Temperature measurement with a sonic anemometer and its application to heat and moisture fluxes. *Boundary-Layer Meteorol* 26:81–93
- Serafin S, Adler B, Cuxart J, Wekker SD, Gohm A, Grisogono B, Kalthoff N, Kirshbaum D, Rotach M, Schmidli J, Stiperski I, Vecenaj Željko, Zardi D (2018) Exchange processes in the atmospheric boundary layer over mountainous terrain. *Atmosphere* 9:102
- Sigmund A, Dujardin J, Comola F, Sharma V, Huwald H, Melo DB, Hirasawa N, Nishimura K, Lehning M (2022) Evidence of strong flux underestimation by bulk parametrizations during drifting and blowing snow. *Boundary-Layer Meteorol* 182:119–146
- Stiperski I, Rotach MW (2016) On the measurement of turbulence over complex mountainous terrain. *Boundary-Layer Meteorol* 159:97–121
- Stull RB (1988) An introduction to boundary layer meteorology. Springer, Dotrich
- Taylor GI (1938) The spectrum of turbulence. *Proc R Soc Ser A Math Phys Sci* 164:476–490
- Urfer-Henneberger C (1970) Neuere beobachtungen über die entwicklung des schönwetterwindsystems in einem v-förmigen alpental (dischmatal bei davos). *Arch Meteorol Geophys Bioklim Ser B* 18:21–42
- van der Valk LD, Teuling AJ, Girod L, Pirk N, Stoffer R, van Heerwaarden CC (2022) Understanding wind-driven melt of patchy snow cover. *Cryosphere* 16:4319–4341
- Vickers D, Mahrt L (2003) The cospectral gap and turbulent flux calculations. *J Atmos Ocean Technol* 20:660–672
- Wever N, Comola F, Bavay M, Lehning M (2017) Simulating the influence of snow surface processes on soil moisture dynamics and streamflow generation in an alpine catchment. *Hydrol Earth Syst Sci* 21:4053–4071
- Whiteman CD, Doran JC (1993) The relationship between overlying synoptic-scale flows and winds within a valley. *J Appl Meteorol* 32:1669–1682
- Zardi D, Whiteman CD (2013) Diurnal mountain wind systems. In: Chow FK, Wekker SFD, Snyder BJ (eds) *Mountain weather research and forecasting*. Springer, Dotrich, pp 35–119
- Zilitinkevich SS, Elperin T, Kleorin N, Rogachevskii I (2007) Energy- and flux-budget (EFB) turbulence closure model for stably stratified flows. Part I: steady-state, homogeneous regimes. *Boundary-Layer Meteorol* 125(2):167–191
- Zängl G (2009) The impact of weak synoptic forcing on the valley-wind circulation in the alpine inn valley. *Meteorol Atmos Phys* 105:37–53

Publisher's Note Springer Nature remains neutral with regard to jurisdictional claims in published maps and institutional affiliations.